Journal of Materials Chemistry A

PAPER

View Article Online
View Journal | View Issue





Cite this: J. Mater. Chem. A, 2019, 7, 12645

# A $Li_2CuPS_4$ superionic conductor: a new sulfide-based solid-state electrolyte†

Zhenming Xu, Ronghan Chen and Hong Zhu *

Received 2nd February 2019
Accepted 15th April 2019

DOI: 10.1039/c9ta01317b

rsc.li/materials-a

A new sulfide-based superionic conductor, a kesterite-structured $Li_2CuPS_4$ (LCPS) material, was proposed based on density functional theory (DFT) calculations. Our theoretical studies reveal that the LCPS material is thermodynamically and dynamically stable, and very likely to be experimentally synthesized. LCPS can form electronically insulating but ionically conducting interphases at high lithium chemical potential, preventing further reduction or oxidation by passivating its surface and enhancing its electrochemical stability due to the limited kinetics. LCPS is a superionic conductor, exhibiting a much higher ionic conductivity of 84.9 mS $cm^{-1}$ at 300 K than the state-of-the-art $Li_{10}GeP_2S_{12}$ material, due to the weaker Li ion binding and the energy compensation for forming Li vacancies due to the variable valence state of the $Cu^+$ cation. The LCPS superionic conductor is promising for use as a solid-state electrolyte material for all-solid-state lithium ion batteries. Moreover, an alternative design principle for fabricating new superionic conductors with Li tetrahedral occupation by reducing the electronegativity difference between the anion element and non-lithium cation elements was identified for the first time.

## Introduction

Lithium-ion batteries (LIBs) provide a lightweight energy-storage solution, enabling many of today's high-tech devices from cell phones to electric cars. Despite current LIBs being generally safe, the accidents of the Boeing 787 Dreamliner battery explosion in 2013 and Samsung cell phones catching fire have compelled the battery industry to replace the liquid components used in the commercial LIBs with solid materials. Solid-state electrolytes (SSEs) are attracting more and more attention from researchers worldwide, due to their natural advantages such as high thermal stability, wide electrochemical windows, and good compatibility with Li metal anodes.[1–3] Furthermore, the direct stacking of solid-state cells in one package achieves a high operating voltage with a smaller volume, which is especially favorable for vehicle applications. Therefore, the SSEs are promising to replace the commercial liquid organic electrolytes and effectively increase the safety and energy density of the all-solid-state lithium ion batteries (ASSLIBs)[4] when combined with Li metal anodes. High Li ionic conductivity (>$10^{-2}$ S $cm^{-1}$) at room temperature is key for SSE materials predominantly used for ASSLIBs.

Recently, inorganic sulfide-based lithium ionic conductor materials with higher ionic conductivities than inorganic oxide-based and organic polymer ones, excellent mechanical strength, good mechanical flexibility, negligible grain-boundary resistances and convenience of synthesis at low temperatures have been widely studied.[5–7] In 2011, Kamaya *et al.*[6] reported a fast ion conductor material applied for solid-state LIBs, Lithium Germanium Phosphorous Sulfide (LGPS) $Li_{10}GeP_2S_{12}$, which exhibits an excellent Li ion conductivity of 12 mS $cm^{-1}$ at room temperature and a wide electrochemical window of 5 V in experiments. However, the high cost of germanium is an obstacle for the large-scale application of the LGPS material. This motivates us to search for other SSE materials with earth-abundant elements that can achieve a better balance between material costs and electrochemical performance, *e.g.* high ionic conductivity, wide electrochemical stability windows, and good chemical and thermal stability with electrodes. Recently, Ceder *et al.* theoretically designed a new superionic conductor of $Li_{1+2x}Zn_{1-x}PS_4$ using cheap zinc metal, which exhibited exceptionally high lithium-ion conductivities of more than 50 mS $cm^{-1}$ at room temperature.[8] But the experimentally synthesized $Li_{1+2x}Zn_{1-x}PS_4$ exhibited a relatively low ionic conductivity of 0.57–0.84 mS $cm^{-1}$ at room temperature,[9,10] and the considerable discrepancy between the measured and predicted conductivities may be due to the Li–Zn disordered states and low crystallinity. G. Hautier *et al.* reported another cheap superionic conductor of $LiTi_2(PS_4)_3$ from experimental characterization to theoretical analysis, which exhibits an excellent lithium ionic conductivity of 6.1 mS $cm^{-1}$ at 300 K, comparable to that of the current state-of-the-art superionic conductors.[11]

In this work, we proposed a kesterite-structured $Li_2CuPS_4$ sulfide material based on density functional theory (DFT) calculations, which is a powerful tool for the study and

*University of Michigan–Shanghai Jiao Tong University Joint Institute, Shanghai Jiao Tong University, 800, Dongchuan Road, Shanghai, 200240, China. E-mail: hong.zhu@sjtu.edu.cn*

† Electronic supplementary information (ESI) available. See DOI: 10.1039/c9ta01317b

computational screening of advanced battery materials.[12,13] The proposed LCPS with lower material cost due to using the earth-abundant copper element rather than germanium exhibits a much higher predicted ionic conductivity of 84.9 mS $cm^{-1}$ at 300 K than LGPS, which can be traced back to the small electronegativity difference between the anion element and non-lithium cation elements. Such a design principle which reduces the coulombic interaction between the anion element and non-lithium cation elements can be applied to the design of new lithium, sodium or multivalent ion superionic conductors.

## Computational methodologies

All calculations were carried out by using the projector augmented wave method[14] in the framework of DFT,[15] as implemented in the Vienna *ab initio* Simulation Package (VASP). The generalized gradient approximation (GGA)[16] and Perdew–Burke–Ernzerhof exchange functional[15] are used. Structural relaxations and electronic structure calculations were performed by using the spin-polarized GGA method.[17] After convergence tests, the plane-wave energy cutoff is set to 500 eV. The Monkhorst–Pack method[18] with $5 \times 5 \times 3$ and $11 \times 11 \times 5$ *k*-point meshes is employed for the Brillouin zone sampling of LCPS, respectively for the structural relaxation and electronic structure calculations. The convergence criteria of energy and force are set to $10^{-5}$ eV per atom and 0.01 eV $Å^{-1}$, respectively.

Zhu *et al.* developed an efficient computational screening strategy combining the topological analysis with *ab initio* molecular dynamics (AIMD) simulations to rapidly search for candidates likely to satisfy the stringent conductivity requirements of lithium superionic conductors.[13] In this work, we also adopted this technological process for the study of LCPS. The compositional phase diagrams and Li grand potential phase diagrams are constructed by using the Pymatgen code based on DFT ground state energies from the Materials Project database.[19,20] Phonon calculations were performed with $2 \times 2 \times 1$ supercells based on the density functional perturbation theory,[21] as implemented in the Phonopy code.[22] Activation energy barriers of Li ion migration are calculated by the climbing image nudged elastic band (CI-NEB) method[23] and AIMD simulations.[3] To maintain the computational cost at a reasonable level, a smaller plane wave energy cut-off of 300 eV is chosen for AIMD simulations of the LCPS $2 \times 2 \times 1$ supercell with gamma-centered *k*-point grids. The time step is set to 2 fs, and LCPS supercell systems were simulated for 100 000 steps with a total time of 200 ps in a statistical ensemble with a fixed particle number, volume, and temperature (NVT), and the last 180 ps simulations were regarded as the equilibrium states for mean square displacement (MSD) analysis.

## Results and discussion

### Determination of the kesterite-type structured $Li_2CuPS_4$

Our previous studies of the $I\bar{4}2d$-$LiMS_2$ (M = Cr, Mn, Fe, Co and Ni) show that they are lithium superionic conductors with very low Li diffusion energy barriers (less than 143 meV),[24] and the smaller electronegativity difference between transition metals and sulfur element results in the low activation barriers. However, the above $I\bar{4}2d$-$LiMS_2$ compounds are metallic due to the conducting $MS_4$ tetrahedron forming electronic transport channels in terms of the spatial structure (Fig. S1†), which is not suitable for SSE materials. By further structure design and element substitution, the ternary $I\bar{4}2d$-$LiMS_2$ compounds would be extended to quaternary compounds to achieve performance balance between electronic and ionic conducting abilities. By introducing insulating $PS_4$ tetrahedra to block the electronic transport channel (Fig. S1†) and considering the small electronegativity difference between P and S elements, we replaced two TM atoms in the $I\bar{4}2d$-$LiMS_2$ unit cell with Cu + P pairs, resulting in a new $Li_2CuPS_4$ (LCPS) compound (space group: $I\bar{4}$). Our proposed LCPS has a body centered tetragonal lattice structure, like the kesterite structured $Cu_2ZnSnS_4$ material.[25] As shown in Fig. 1a, each lithium, copper and phosphorus atom is bonded to four sulfur atoms forming tetrahedra and each sulfur atom is tetrahedrally coordinated to two lithium atoms, one copper atom and one phosphorus atom. There are two inequivalent Li sites in LCPS, Li site-1 in the Cu atom layer and Li site-2 in the P atom layer. We also note that there are two fundamental structures coexisting in the synthesized $Cu_2ZnSnS_4$ samples with a negligible energy difference of 3 meV per atom,[26] including kesterite and stannite structures (space group: $I\bar{4}2m$). Therefore, in this work we have also evaluated the different phase structures with the same $Li_2CuPS_4$ formula, including kesterite, stannite, and primitive mixed CuAu-like structures. Table S1† shows that the kesterite structured LCPS is in the ground state with the lowest energy, and the energy difference between the kesterite and stannite structure is 29 meV per atom, which is close to the $k_BT$ of ~26 meV per atom at room temperature. This indicates that kesterite and stannite ordering may coexist in the synthesized samples. However, the primitive mixed CuAu-like structure is much less likely to coexist with the kesterite ordering due to its relatively larger energy difference. In the following calculations, we focused on the ground state kesterite structured LCPS to efficiently evaluate its application potential for the SSE material, and the stannite structured LCPS will be further studied in other work. The optimized lattice constants, atomic coordinates and simulated X-ray diffraction (XRD) pattern of LCPS are summarized and shown in Table S2 and Fig. S2a in the ESI,† respectively. Moreover, for the convenience of experimental structural characterization, the calculated Raman spectrum and the characteristic vibration modes of LCPS are also provided in Fig. S2.†

### Evaluation of LCPS stability

First, the feasibility of the experimental synthesis of the new LCPS was systematically assessed from its thermodynamic and dynamic stabilities. The thermodynamic stabilities of LCPS were studied by constructing DFT calculated Li–Cu–P–S quaternary compositional phase diagrams, as shown in Fig. 1b. Any red dot in the phase diagram represents a stable compound at the DFT level whose energy is lower than that of any other compound or the linear combination of compounds of that composition. The Li–Cu–P–S phase diagram shows that the

 

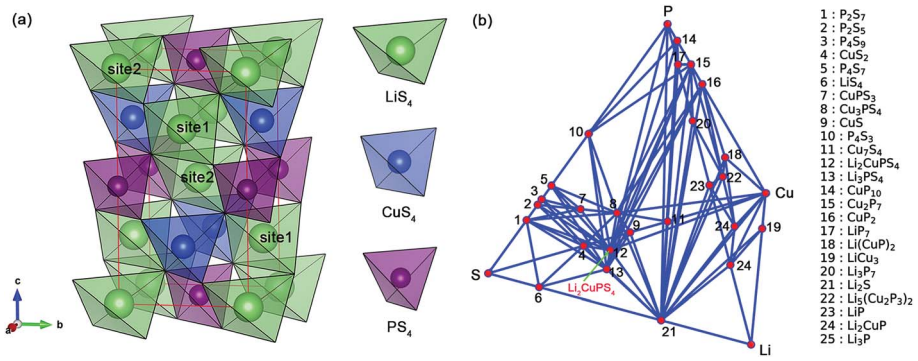


Fig. 1 3D structural plot of (a) the unit cell of a kesterite-structured $Li_2CuPS_4$ crystal and (b) DFT calculated phase diagrams of the Li–Cu–P–S quaternary system; the red dots represent stable compounds (the $Li_2CuPS_4$ compound is stable in this quaternary system).

LCPS compound is thermodynamically stable and can hopefully be synthesized by the spontaneous reaction of its phase equilibrium compounds, *e.g.* $Li_3PS_4$ and $Cu_3PS_4$. The DFT calculated formation energy of the LCPS compound is −0.031 eV f.u.$^{-1}$ with respect to the ground state $Li_3PS_4$ and $Cu_3PS_4$, as depicted in the $Li_3PS_4$–$Cu_3PS_4$ pseudo-binary phase diagram in Fig. S3.† We expect that the actual formation energy of the LCPS compound at elevated temperatures could be lower than −0.031 eV f.u.$^{-1}$ due to entropic contributions. No imaginary vibrational mode is observed from the phonon dispersion spectrum of the $I\bar{4}$ LCPS (Fig. S4†), which indicates that LCPS is dynamically stable. Moreover, the elastic constants of LCPS were calculated to verify its mechanical stability.[27] According to the Born elastic theory,[28] the elastic constant constitutes a symmetric 6 × 6 tensor matrix in the linear elastic range. Due to symmetry, the independent elastic constants are reduced to 7 values for the orthorhombic LCPS crystal. The calculated elastic constants are summarized in Table S3 in the ESI.† All these elastic constants comply well with the Born criteria for the mechanically stable tetragonal crystal,[29] which are $C_{11} > |C_{12}|$, $C_{33}(C_{11} + C_{22}) > 2C_{13}^2$, $C_{44} > 0$, and $C_{66}(C_{11}–C_{22}) > 2C_{16}^2$, confirming the mechanical stabilities of LCPS material at the DFT level. In addition, the elastic properties of electrolyte materials are crucial parameters for designing SSLIBs.[30] The bulk modulus of the crystal material is associated with elastic resistance to atomic bond stretching, and the shear modulus represents resistance to plastic deformation under external stress. Therefore, the ratio of $B/G$ is regarded as an important parameter measuring the dominant elasticity or plasticity of a crystal material.[31] Ductile materials usually have a high $B/G$ ratio value (more than 1.75), whereas a small value (less than 1.75) is representative of a brittle material.[32] The LCPS material has good ductility with a $B/G$ ratio of 2.16. From the comparison in Table S3,† all the calculated $B$, $E$, and $G$ moduli of LCPS are much larger than those of Li metal[29] and even the $Li_3PS_4$ electrolyte,[33] suggesting that LCPS may effectively block the growth of lithium dendrites and has good mechanical contact at the electrode/SSE interface. Based on the thermodynamic, dynamic and mechanical stabilities, we can conclude that LCPS is stable and can be promising for experimental synthesis.

## Electrochemical stability

**Intrinsic stability against inert electrodes.** In a battery, electronic conduction across the electrolyte must be minimal. So, we determined the LCPS band gap to assess its electronic insulation and intrinsic redox stabilities against the inert electrodes or the upper boundary of the electrochemical window, which can be regarded as the voltage range where the material is neither oxidized nor reduced.[34] The calculated spin-polarized band structure and element-projected density of states (PDOS) of the LCPS compound with the Heyd–Scuseria–Ernzerhof (HSE06) screened hybrid functional[35] are shown in Fig. 2. It can be seen from Fig. 2a that the spin-up and -down bands are identical, indicating that LCPS is a nonmagnetic material. The HSE06 hybrid functional calculated band gap of LCPS is 3.30 eV, slightly smaller than the 3.6 eV of LGPS.[36] The LCPS intrinsic electrochemical window is narrower than the electrode potential of the high voltage oxide-type cathode, but may cover the electrode potential of sulfide-type cathodes, such as $TiS_2$. We expect that the actual electrochemical window of LCPS could be further extended by forming passivating interface layers, which can effectively prevent the electrolyte from being further oxidized or reduced and hence enhance the kinetic stabilities, like the kinetically stable LGPS with an electrochemical window of ∼5 V.[6,37] In addition, the PDOS in Fig. 2b shows that the valence band maximum of LCPS is dominated by the d states of $Cu^+$ cations and the p states of $S^{2-}$ anions. This means that $Cu^+$ cations and $S^{2-}$ anions are the first species to be oxidized at high voltages. And the conduction band minimum of LCPS is dominated by the p states of $S^{2-}$ anions and the s states of $P^{5+}$ cations, but only $P^{5+}$ cations can be reduced first at low voltages. Such results only provide an upper boundary of electrochemical stabilities and further analyses at the electrode potential are needed.

**Extrinsic stability against electrodes.** When SSE materials come into contact with the Li anode and high voltage cathode during cycling operations of solid-state lithium batteries, at the anode side, the high lithium chemical potential makes the electrolyte undergo reduction with Li insertion. And the electrolyte, at the charged cathode side in a strongly oxidizing environment (low lithium chemical potential), would be

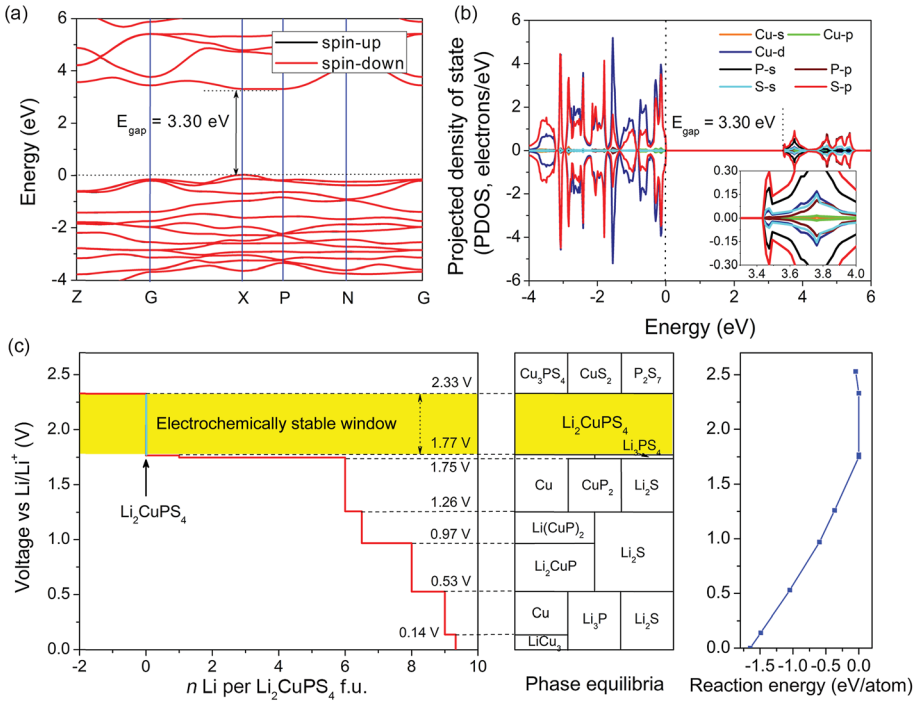


Fig. 2 HSE06 hybrid functional calculated (a) spin-polarized band structure (the spin-up and -down are the same), and (b) orbital-projected density of electron states (PDOS) of the $Li_2CuPS_4$ primitive cell, where the Fermi level is shifted to zero and the PDOS of Li atoms is not shown due to their weak distribution in this energy region. (c) DFT calculated voltage profiles, phase equilibria and decomposition reaction energy of $Li_2CuPS_4$ upon lithiation ($n > 0$) and delithiation ($n < 0$).

strongly oxidized with Li extraction.[38,39] Thus, lithium grand potential phase diagrams, representing the phase equilibrium systems that are in equilibrium with the Li metal electrode or the applied lithium potential,[40] were constructed to evaluate the electrochemical stability of LCPS material. Based on the constructed lithium grand potential phase diagrams of Li–Cu–P–S quaternary systems, the DFT calculated voltage profiles, phase equilibria and decomposition reaction energies of LCPS upon lithiation and delithiation are depicted in Fig. 2c. It can be observed that LCPS will be oxidized to $Cu_3PS_4$, $CuS_2$ and $P_2S_7$ phases with much Li extraction when the voltage is higher than 2.33 V. On the other hand, LCPS will undergo reduction starting at 1.77 V, where LCPS is lithiated and transforms into Cu and $Li_3PS_4$ phases. At 1.75 V, the formed $Li_3PS_4$ combined with LCPS begins to be further reduced into Cu, $CuP_2$ and $Li_2S$ phases. With the further decrease of the voltage, there are multiple thermodynamic equilibria with more favorable reaction energies, corresponding to the Li–Cu–P alloying processes upon lithiation. The final reduction products at 0 V (on the Li metal anode side) of LCPS are $LiCu_3$, $Li_3P$, and $Li_2S$. Therefore, the calculated electrochemical window of LCPS is from 1.77 to 2.33 V, and the corresponding window width is 0.66 V, slightly larger than the 0.43 V of LGPS.[41]

What needs illustration is that the above electrochemical stability analysis of a material from the lithium grand potential phase diagram is purely based on the thermodynamic driving force for the decomposition reaction. The kinetics of the decomposition or redox reaction were not considered, but are known to be important in determining the extent of the decomposition reaction.[41] The morphologies, electronic and ionic conductivities of the decomposition products and the applied current all affect the decomposition reaction kinetics of a material. The experiment reported that the electrochemical stability window of LGPS determined by the cyclic voltammetry technique is 0.0–5.0 V,[6] much wider than the calculated values of 1.7–2.1 V from the lithium grand potential phase diagram.[41] This indicates that the advantageous decomposition products (electronic insulation) of LGPS at both high and low lithium chemical potential contribute to the sluggish kinetics of the decomposition reaction regardless of the favorable decomposition driving force, and passivate the electrolyte surface, significantly extending its experimental electrochemical window.

Much like that for LGPS, the sluggish kinetics of the decomposition reaction may also occur for our LCPS material. At low lithium chemical potential, due to the good electronic insulation properties of the decomposition products of $Cu_3PS_4$ and $P_2S_7$, the formed thin interphases would prevent the LCPS from being further oxidized by passivating its interface with cathode materials. Meanwhile, at very high lithium chemical potential (against the Li metal anode), the LCPS material will be strongly reduced with a reaction energy of $\sim$−1.6 eV per atom, following the reaction of $9.33Li + Li_2CuPS_4 \Rightarrow 0.33LiCu_3 + Li_3P + 4Li_2S$. Although the presence of metallic Li–Cu alloys in the decomposition products is worrisome and may accelerate the decomposition kinetics, the quantity of the formed electronically insulating $Li_3P$ (band gap is 2.03 eV)[42,43] and $Li_2S$ (band gap is 5.0 eV)[44] phases is about 15 times more than that of the

 

metallic $LiCu_3$ alloy, corresponding to a volume fraction of ~4%, much smaller than the ~12% of $Li_{15}Ge_4$ in the reduction interphases of LGPS at a low voltage. This means that the $LiCu_3$ alloy is dispersed in the electronically insulating $Li_3P$ and $Li_2S$ glass phases, and the complete 3D electronically conducting pathways are not likely to occur due to the small volume fraction of $LiCu_3$,[45] so all the decomposition product composites are very likely to be electronically insulating. The microstructure of these formed solid-state interphases should be further verified by experimental study. On the other hand, the formed $Li_3P$ and $Li_2S$ phases are electrochemically stable against Li metal[38] and show relatively good Li ion diffusion abilities.[46,47] Hence, although the LCPS material is thermodynamically not stable at very high and low lithium chemical potential, the electronically insulating but ionically conducting interphases can effectively passivate the LCPS surface and enhance its electrochemical stability to a certain extent due to the limited kinetics of the decomposition reaction.

To possibly apply LCPS in solid-state lithium batteries, here, we proposed three methods to improve its extrinsic electrochemical stability by reducing the decomposition reaction driving force. The first method is to use intermediary Li alloys, such as Li–Sn[48] and Li–Al,[49] as a buffer layer to reduce the lithium chemical potential at the LCPS surface forming a Li/Li–Sn(Al)/LCPS sandwich structure. The second method is sulfurizing the Li metal surface with $H_2S$ gas to form a thin electronically insulating $Li_2S$ layer with a spontaneous reaction, artificially constructing $Li/Li_2S$/LCPS multiple interfaces. The last strategy is coating the LCPS electrolyte with Li ion conducting $Li_3N$,[50] which not only shows excellent interfacial stabilities with Li metal anodes,[38] but can also effectively prevent the LCPS electrolyte from being directly reduced by Li metal.

### Lithium ion diffusivity and conductivity

High ionic conductivities larger than $10^{-2}$ S $cm^{-1}$ at room temperature are critical requirements for the practical application of SSEs in ASSLIBs. In this section, the Li ion diffusivity and conductivity of the LCPS material were investigated by CI-NEB calculations and AIMD simulations.[12] Defects in a material have significant influences on ion transport, and the synthesis environment (*e.g.* element chemical potential) determines the types of defects in a material by affecting their formation energies. Thus, to guide future experiments, it is essential to figure out what synthesis environment and what types of defects are beneficial for Li ion diffusion in the LCPS material. In this work, we considered three types of Li point defects in LCPS based on the $2 \times 2 \times 1$ supercell models, including the neutral and charged Li vacancies ($V_{Li}$ and $V_{Li}^-$), neutral and charged interstitial Li ($Li_i$ and $Li_i^+$, at both the tetrahedral and octahedral interstitial sites), and Li Frenkel vacancy–interstitial pairs ($Li_{Fr}$, at both the tetrahedral and octahedral center interstitial sites) (see details in Fig. S5†). By the widely used calculation methods of defect formation energy (see details in the ESI†),[47,51] the Li point defect formation energies at both low and high lithium chemical potentials ($\Delta\mu_{Li} = -2.33$ eV, oxidation potential; $\Delta\mu_{Li} = -1.77$ eV, reduction potential) with respect to different Fermi energy levels of LCPS were calculated, and the results are shown in Fig. 3. They show that the neutral and charged Li vacancy formation energies of LCPS are much lower than those of the other defects, indicating that Li vacancies are the dominant defects in the LCPS material. We also observe that both the neutral and charged Li interstitial defect formation energies of the tetrahedral interstitial sites are lower than those of the octahedral interstitial sites, demonstrating that Li ions prefer to occupy the tetrahedral interstitial sites to form $LiS_4$ tetrahedra.

Then, the energy barrier of a single Li vacancy diffusion in LCPS was calculated by the CI-NEB method, as shown in Fig. 4a. There is only one Li vacancy-hopping path (site-1 ↔ site-2) between two adjacent Li sites (site-1 and site-2). The Li vacancy hopping path from one Li site-1 to another Li site-1 or one Li site-2 to another Li site-2 should go through two octahedral and one tetrahedral interstitial site, which is much longer than the site-1 ↔ site-2 path and is less likely to occur. Hence, only the Li vacancy-hopping path along site-1 ↔ site-2 was considered for CI-NEB calculations in this work. It is found that Li ions prefer to occupy site-2 with a more favorable energy of −0.083 eV per atom than that of the site-1, because these two Li sites are surrounded by different second nearest neighbors (Li site-1 is in the Cu atom layer, while Li site-2 is in the P atom layer, Fig. 1a). When Li diffuses from site-1 to site-2, it goes through a transition state at the octahedral interstitial site (Fig. 4a) with a small activation energy barrier of 122 meV, while for Li diffusing along the reverse direction (from site-2 to site-1), there is a relatively high energy barrier of 205 meV. We expect that the average energy barrier for Li diffusion in LCPS is in the range of 122–205 meV. For comparison, we have also calculated the energy barriers of Li interstitial diffusion along different paths in LCPS, as shown in Fig. S6.† The calculated energy barriers of Li interstitial diffusion are in the range of 400–900 meV, much larger than those of Li vacancy diffusion. Therefore, the ionic conduction of LCPS is mainly contributed by Li vacancies due to their more favorable formation energies and lower diffusion energy barriers.

On the other hand, AIMD simulations were performed to further understand Li diffusion in LCPS and verify the foregoing results from CI-NEB calculations. To accelerate the convergence of the diffusion coefficient and reduce the computational costs, our AIMD simulations were carried out at elevated temperatures from 500 to 900 K. Fig. 4b shows the Arrhenius plot for the various Li ion diffusion coefficients with respect to five different elevated temperatures of LCPS in comparison with LGPS. The Li ion diffusion coefficients of LCPS are much larger than those of LGPS at the same temperature. We calculated an overall activation barrier of 142 meV for Li vacancy diffusion in LCPS, which is in good agreement with the energy barrier of 122–205 meV determined by CI-NEB calculations. Encouragingly, this calculated energy barrier of Li vacancy diffusion in LCPS is smaller than the AIMD calculated 210–240 meV of LGPS,[6,36] 320–400 meV of β-$Li_3PS_4$ (LPS),[52,53] 181–252 meV of $Li_{1+2x}Zn_{1-x}PS_4$ ($x = 0.25$ and 0.5)[8] and 278 meV of $Li_3Y(PS_4)_2$,[13] indicating that the ionic conductivity of LCPS is superior to that of most sulfide materials. The extrapolated Li ion diffusion

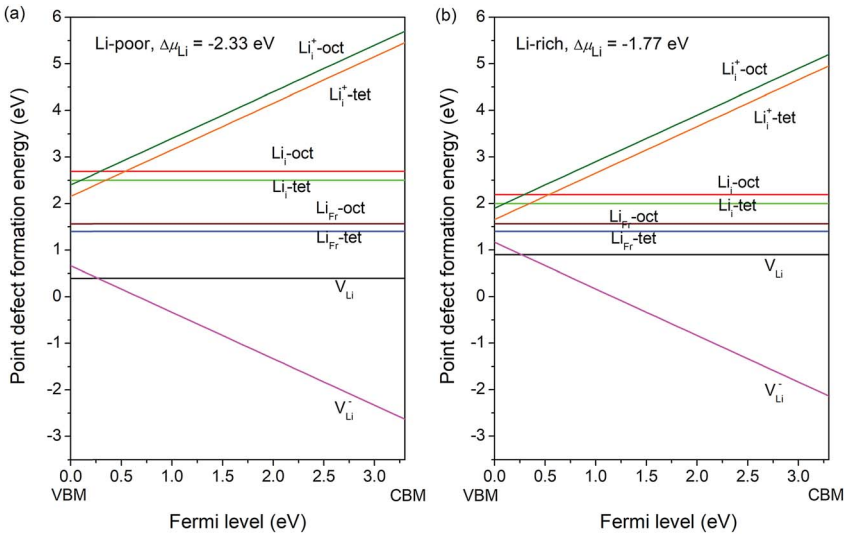


Fig. 3 Defect formation energies of $Li_2CuPS_4$ with neutral and charged Li vacancies, neutral and charged Li interstitial sites (tetrahedral and octahedral center sites) and neutral and charged Li Frenkel vacancy–interstitial pairs (tetrahedral and octahedral center interstitial sites) as a function of the Fermi energy level (a) under Li poor conditions ($\Delta\mu_{Li} = -2.33$ eV, the starting oxidation potential of LCPS) and (b) under Li rich conditions ($\Delta\mu L_i = -1.77$ eV, the starting reduction potential of LCPS).

coefficient at 300 K from the Arrhenius plot (Fig. 4b) is estimated to be $1.13 \times 10^{-6}$ cm$^2$ s$^{-1}$, and the room temperature Li ion conductivity is 84.9 mS cm$^{-1}$, much larger than the 9 mS cm$^{-1}$ of LGPS,[36] 3.4–27.7 mS cm$^{-1}$ of $Li_{1.5}Zn_{0.75}PS_4$,[8] 2.2 mS cm$^{-1}$ of $Li_3Y(PS_4)_2$ (ref. 13) and even 57 mS cm$^{-1}$ of $Li_7P_3S_{11}$ (ref. 54) from AIMD simulations. The MSDs of Li ions in Fig. 4c show that diffusion in LCPS is anisotropic, and the MSDs in the $z$ direction are about two times larger than those in the $x$ and $y$ directions, indicating that Li ion diffusion along the $z$ direction is easier than that along the $x$–$y$ plane direction. There are nonetheless significant Li ion diffusion in the $x$–$y$ plane as well, which is still comparable with that of the state-of-the-art solid electrolytes. It can be seen from the atomic trajectories in Fig. 4d that the S anion frameworks are well maintained and no

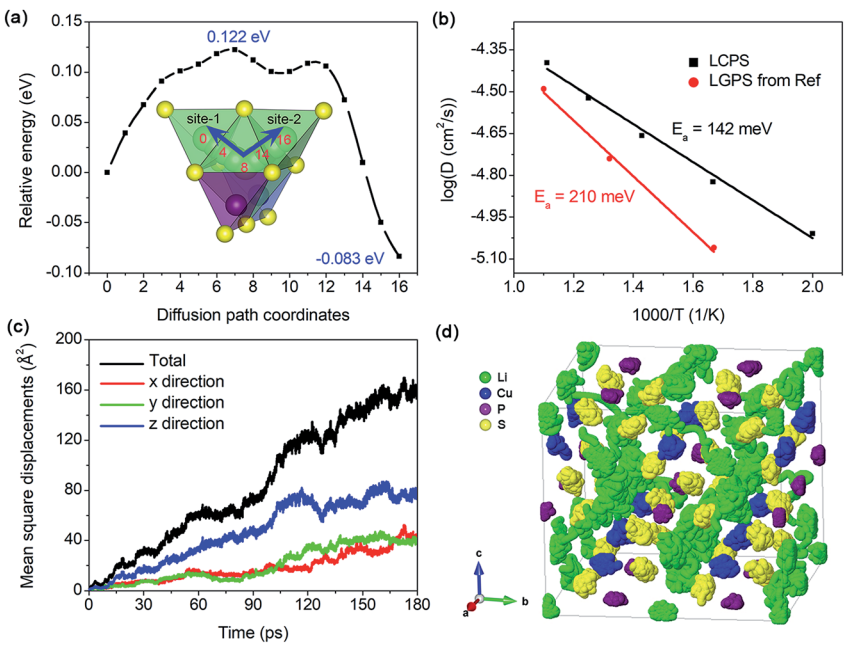


Fig. 4 Li ion diffusivity and conductivity of LCPS. (a) Energy variations of Li ion migration by the vacancy diffusion mechanism from one tetrahedral site to its adjacent tetrahedral site through a transition state at the octahedral interstitial site in LCPS, (b) Arrhenius plot of the Li ion diffusion coefficient of LCPS, (c) total and axial MSDs of Li from 600 K AIMD simulations, and (d) 3D visualization of the atomic trajectories from 600 K AIMD simulations of LCPS $2 \times 2 \times 1$ supercell structures with 6.25% vacancy defects (molar concentration), the atomic trajectories were displayed using the Jmol code.[55]

 

breaking of P–S or Cu–S bonds is observed during the whole 600 K AIMD simulation. Moreover, atomic trajectories clearly exhibit significant Li hopping in the $x$–$y$ plane direction. Our CI-NEB calculations and AIMD simulations demonstrate that LCPS is a 3D superionic conductor, whose room temperature ionic conductivity is much superior to that of the state-of-the-art sulfide-type solid electrolytes, such as LGPS and LPS.

We wonder why our LCPS material can exhibit such exceptionally excellent Li ion diffusion performances. Recently, Ceder *et al.* proposed an important design principle of superionic conductors in which a bcc anion framework with face-sharing $LiS_4$ tetrahedra for optimal Li diffusion allows the lowest activation energy barrier of Li diffusion,[56] *e.g.* LGPS and $L_7P_3S_{11}$. Although the sulfur atom sublattices of LCPS can be approximately matched to a fcc anion framework (Fig. 1a), the adjacent $LiS_4$ tetrahedra in LCPS are point-sharing (two tetrahedra are connected by a sulfur atom) rather than face-sharing as seen in LGPS. Thus, we note that there are some other factors which synthetically contribute to such exceptionally excellent Li ion diffusion ability in LCPS.

The experimentally measurable activation barrier is the sum of the migration enthalpy and the defect formation enthalpy.[57,58] First, we find that the formation energies of a neutral $V_{Li}$ and a charged $V_{Li}^-$ vacancy in LCPS are 0.50 and 0.21 eV lower than those in LGPS for the same Li chemical potential, respectively (Fig. S7†), indicating that Li ion binding in LCPS is weaker than that in LGPS. Such a difference in Li ion binding strength in LCPS and LGPS could be traced back to the Li–S coulombic interactions, which are proportional to the charge and the reciprocal of the bond length. The Bader charges of the S anion ($q_S$) are calculated to be $-0.85e$ and $-1.05e$ for LCPS and LGPS, respectively, and the average Li–S bond lengths ($d_{Li-S}$) of LCPS and LGPS are 2.47 and 2.69 Å, respectively. Therefore, the $q_S/d_{Li-S}$ for LCPS is 0.34, slightly smaller than 0.39 of LCPS, indicating that the coulombic interactions between mobile $Li^+$ ions and S anion frameworks in LCPS are weaker than those in LGPS, which is consistent with the above formation energy results of Li vacancies. Our previous studies on the chalcopyrite-structured $LiMS_2$ (M represents 3d transition metals) materials show that the weaker coulombic interaction between mobile $Li^+$ ions and S anion frameworks induced by the smaller difference of electronegativities between M and S elements (Li–S bond lengths are almost the same) leads to lower migration enthalpy.[24] In addition, Ning *et al.* studied the Jahn–Teller-distortion tuned Li-ion migration in λ-$MnO_2$ and also claimed that the Coulomb interaction between Li and the neighboring O ions is the main contribution to the migration barrier.[59] It could also be noted that similar effects have been found in $Li_{10}Ge_{1-x}Sn_xP_2S_{12}$, in which the longer $Sn^{4+}$–$S^{2-}$ bonds and lower electronegativity of Sn *vs.* Ge (1.7 *vs.* 2.0, Allred–Rochow scale of electronegativity) give rise to higher electron density on the $S^{2-}$ atoms in Sn-rich compounds, which leads to stronger $Li^+$–$S^{2-}$ coulombic attractions and thereby increased activation barriers in Sn-rich compounds.[7] Therefore, we can conclude that the weak coulombic interactions weaken Li ion binding with the crystalline framework, and in turn reduce the formation enthalpy and migration enthalpy of Li, consequently lowering the activation barrier and enhancing Li ion diffusion in LCPS. Second, the electron clouds of $Cu^+$ in LCPS are softer than those of $Ge^{4+}$ in LGPS. When forming a Li vacancy in LCPS, its adjacent $Cu^+$ will be oxidized to the high-valence $Cu^{2+}$ to keep local structures electrically neutral (see Bader charges and charge density differences in Table S5 and Fig. S8†), and this process may compensate or be harmless for Li vacancy formation at least, while the rigid $Ge^{4+}$ in LGPS can't be further oxidized when its adjacent $Li^+$ ions are absent (Fig. S8b†), and the local structures will be negatively charged with Coulomb repulsion interactions, increasing the formation energy of vacancy defects to a certain extent.[60,61] This may be another important reason for our LCPS having superior Li ion diffusion than LGPS. Finally, the distorted $LiS_4$ tetrahedra in the LCPS crystalline framework offer energetically unfavorable Li occupying sites (Fig. S9†), leading to relatively flat potential energy landscapes for fast Li diffusion.[11]

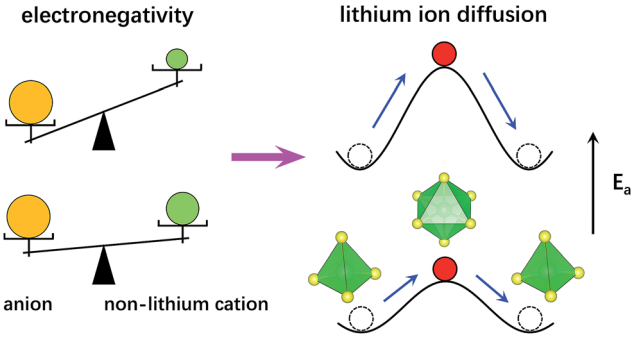


Fig. 5 Schematic illustration of the effect of electronegativity differences between the anion element and non-lithium cation elements on the octahedral Li ion diffusion.

Here, based on the profound understanding of LCPS and our previously reported $LiMS_2$ superionic conductors,[24] we first identified an alternative design principle for superionic conductors with Li tetrahedral occupation in which the small electronegativity difference between the anion element and non-lithium cation elements is essential for achieving excellent fast ion diffusion, as depicted in Fig. 5. Our work provides another efficient method for fabricating new lithium, sodium and also multivalent ion superionic conductors, complementary to the tetrahedral face-sharing design principle.[56]

## Conclusion

In summary, we used the first-principles calculations based on DFT to demonstrate a kesterite-structured LCPS material and its Li ion transport behavior. The feasibility of the experimental synthesis of the LCPS material was estimated using the DFT calculated phase diagram and phonon dispersion spectrum. The electrochemical stability calculations based on the HSE06 calculated density of electron states and Li grand-potential phase diagrams indicate that the LCPS material is thermodynamically not stable at very high or low lithium chemical potentials, but it is possible to form electronically insulating but ionically conducting interphases, preventing the LCPS material

from being further reduced or oxidized by passivating the surface and hence enhancing its electrochemical stability to a certain extent due to the limited kinetics. Based on the inspiring results from the nudged elastic band calculations and *ab initio* molecular dynamics simulations, we characterized the LCPS material as a superionic conductor, which exhibits a much higher ionic conductivity of 84.9 mS $cm^{-1}$ at 300 K than most solid-state electrolyte materials, such as $Li_{10}GeP_2S_{12}$ and $Li_3PS_4$, due to its lower Li ion binding and the energy compensation when forming Li vacancies from the variable valence state of $Cu^+$ cations. Our calculations demonstrate that the LCPS superionic conductor is quite promising for experimental synthesis and use as a solid-state electrolyte material for all-solid-state lithium ion batteries. We first identified an alternative design principle for fabricating new lithium, sodium and also multivalent ion superionic conductors with Li tetrahedral occupation by reducing the electronegativity difference between the anion element and non-lithium cation elements.

## Conflicts of interest

The authors declare no competing financial interest.

## Acknowledgements

This work was supported by the National Natural Science Foundation of China (51602196). All simulations were performed at the Shanghai Jiao Tong University High Performance Computing Center.

## References

1 T. Thompson, S. Yu, L. Williams, R. D. Schmidt, R. Garcia-Mendez, J. Wolfenstine, J. L. Allen, E. Kioupakis, D. J. Siegel and J. Sakamoto, *ACS Energy Lett.*, 2017, **2**, 462–468.
2 X. He, Y. Zhu and Y. Mo, *Nat. Commun.*, 2017, **8**, 15893.
3 Z. Deng, Z. Zhu, I.-H. Chu and S. P. Ong, *Chem. Mater.*, 2017, **29**, 281–288.
4 J. C. Bachman, S. Muy, A. Grimaud, H. H. Chang, N. Pour, S. F. Lux, O. Paschos, F. Maglia, S. Lupart, P. Lamp, L. Giordano and Y. Shao-Horn, *Chem. Rev.*, 2016, **116**, 140–162.
5 M. Tatsumisago, M. Nagao and A. Hayashi, *Journal of Asian Ceramic Societies*, 2013, **1**, 17–25.
6 N. Kamaya, K. Homma, Y. Yamakawa, M. Hirayama, R. Kanno, M. Yonemura, T. Kamiyama, Y. Kato, S. Hama, K. Kawamoto and A. Mitsui, *Nat. Mater.*, 2011, **10**, 682–686.
7 H. Yamane, M. Shibata, Y. Shimane, T. Junke, Y. Seino, S. Adams, K. Minami, A. Hayashi and M. Tatsumisago, *Solid State Ionics*, 2007, **178**, 1163–1167.
8 W. D. Richards, Y. Wang, L. J. Miara, J. C. Kim and G. Ceder, *Energy Environ. Sci.*, 2016, **9**, 3272–3278.
9 N. Suzuki, W. D. Richards, Y. Wang, L. J. Miara, J. C. Kim, I.-S. Jung, T. Tsujimura and G. Ceder, *Chem. Mater.*, 2018, **30**, 2236–2244.
10 K. Kaup, F. Lalère, A. Huq, A. Shyamsunder, T. Adermann, P. Hartmann and L. F. Nazar, *Chem. Mater.*, 2018, **30**, 592–596.
11 D. Di Stefano, A. Miglio, K. Robeyns, Y. Filinchuk, M. Lechartier, A. Senyshyn, H. Ishida, S. Spannenberger, B. Roling and Y. Kato, 2017, arXiv preprint arXiv:1708.02997.
12 G. Ceder, S. P. Ong and Y. Wang, *MRS Bull.*, 2018, **43**, 746–751.
13 Z. Zhu, I.-H. Chu and S. P. Ong, *Chem. Mater.*, 2017, **29**, 2474–2484.
14 P. E. Blöchl, *Phys. Rev. B*, 1994, **50**, 17953–17979.
15 W. Kohn and L. J. Sham, *Phys. Rev. B*, 1965, **140**, A1133–A1138.
16 J. P. Perdew, K. Burke and M. Ernzerhof, *Phys. Rev. Lett.*, 1996, **77**, 3865–3868.
17 S. L. Dudarev, G. A. Botton, S. Y. Savrasov, C. J. Humphreys and A. P. Sutton, *Phys. Rev. B: Condens. Matter Mater. Phys.*, 1998, **57**, 1505–1509.
18 H. J. Monkhorst and J. D. Pack, *Phys. Rev. B: Solid State*, 1976, **13**, 5188–5192.
19 S. P. Ong, W. D. Richards, A. Jain, G. Hautier, M. Kocher, S. Cholia, D. Gunter, V. L. Chevrier, K. A. Persson and G. Ceder, *Comput. Mater. Sci.*, 2013, **68**, 314–319.
20 A. Jain, S. P. Ong, G. Hautier, W. Chen, W. D. Richards, S. Dacek, S. Cholia, D. Gunter, D. Skinner, G. Ceder and K. A. Persson, *APL Mater.*, 2013, **1**, 170901.
21 S. Baroni, S. de Gironcoli, A. Dal Corso and P. Giannozzi, *Rev. Mod. Phys.*, 2001, **73**, 515–562.
22 A. Togo and I. Tanaka, *Scr. Mater.*, 2015, **108**, 1–5.
23 G. Henkelman and H. Jónsson, *J. Chem. Phys.*, 2000, **113**, 9978–9985.
24 Z. M. Xu, S. H. Bo and H. Zhu, *ACS Appl. Mater. Interfaces*, 2018, **10**, 36941–36953.
25 S. K. Wallace, J. M. Frost and A. Walsh, *J. Mater. Chem. A*, 2019, **7**, 312–321.
26 S. Chen, X. G. Gong, A. Walsh and S.-H. Wei, *Appl. Phys. Lett.*, 2009, **94**, 041903.
27 C. S. Liu, H. H. Zhu, X. J. Ye and X. H. Yan, *Nanoscale*, 2017, **9**, 5854–5858.
28 M. Born and K. Huang, *Dynamical Theory of Crystal Lattices*, Oxford University Press, Oxford, 1954.
29 F. Mouhat and F.-X. Coudert, *Phys. Rev. B: Condens. Matter Mater. Phys.*, 2014, **90**, 224104.
30 Z. Deng, Z. Wang, I.-H. Chu, J. Luo and S. P. Ong, *J. Electrochem. Soc.*, 2015, **163**, A67–A74.
31 A. Makishima and J. D. Mackenzie, *J. Non-Cryst. Solids*, 1973, **12**, 35–45.
32 L. Vitos, P. A. Korzhavyi and B. Johansson, *Phys. Rev. Lett.*, 2002, **88**, 155501.
33 Y. Yang, Q. Wu, Y. Cui, Y. Chen, S. Shi, R. Z. Wang and H. Yan, *ACS Appl. Mater. Interfaces*, 2016, **8**, 25229–25242.
34 J. B. Goodenough and Y. Kim, *Chem. Mater.*, 2010, **22**, 587–603.
35 S. P. Ong, Y. Mo, W. D. Richards, L. Miara, H. S. Lee and G. Ceder, *Energy Environ. Sci.*, 2013, **6**, 148–156.
36 Y. Mo, S. P. Ong and G. Ceder, *Chem. Mater.*, 2011, **24**, 15–17.

 

37 T. Kobayashi, A. Yamada and R. Kanno, *Electrochim. Acta*, 2008, **53**, 5045–5050.
38 Y. Zhu, X. He and Y. Mo, *ACS Appl. Mater. Interfaces*, 2015, **7**, 23685–23693.
39 Y. Zhu, X. He and Y. Mo, *J. Mater. Chem. A*, 2016, **4**, 3253–3266.
40 S. Ping Ong, L. Wang, B. Kang and G. Ceder, *Chem. Mater.*, 2008, **20**, 1798–1807.
41 F. Han, Y. Zhu, X. He, Y. Mo and C. Wang, *Adv. Energy Mater.*, 2016, **6**, 1501590.
42 M. Seel and R. Pandey, *Solid State Ionics*, 1992, **53–56**, 924–927.
43 M. Seel and R. Pandey, *Int. J. Quantum Chem.*, 1991, **40**, 461–478.
44 B. S. Kim, M. S. Lee, K. Y. Park and K. Kang, *Chem.–Asian J.*, 2016, **11**, 1288–1292.
45 S. Kirkpatrick, *Rev. Mod. Phys.*, 1973, **45**, 574–588.
46 G. Nazri, *Solid State Ionics*, 1989, **34**, 97–102.
47 A. Moradabadi and P. Kaghazchi, *Appl. Phys. Lett.*, 2016, **108**, 213906.
48 Z. Li, J. Ding and D. Mitlin, *Acc. Chem. Res.*, 2015, **48**, 1657–1665.
49 K. K. Fu, Y. Gong, B. Liu, Y. Zhu, S. Xu, Y. Yao, W. Luo, C. Wang, S. D. Lacey, J. Dai, Y. Chen, Y. Mo, E. Wachsman and L. Hu, *Sci. Adv.*, 2017, **3**, 1601659.
50 W. Li, G. Wu, C. M. Araújo, R. H. Scheicher, A. Blomqvist, R. Ahuja, Z. Xiong, Y. Feng and P. Chen, *Energy Environ. Sci.*, 2010, **3**, 1524–1530.
51 S. Zhang and J. Northrup, *Phys. Rev. Lett.*, 1991, **67**, 2339–2342.
52 N. H. H. Phuc, M. Totani, K. Morikawa, H. Muto and A. Matsuda, *Solid State Ionics*, 2016, **288**, 240–243.
53 K. Hayamizu, Y. Aihara, T. Watanabe, T. Yamada, S. Ito and N. Machida, *Solid State Ionics*, 2016, **285**, 51–58.
54 I. H. Chu, H. Nguyen, S. Hßy, Y. C. Lin, Z. Wang, Z. Xu, Z. Deng, Y. S. Meng and S. P. Ong, *ACS Appl. Mater. Interfaces*, 2016, **8**, 7843–7853.
55 R. M. Hanson, *J. Appl. Crystallogr.*, 2010, **43**, 1250–1260.
56 Y. Wang, W. D. Richards, S. P. Ong, L. J. Miara, J. C. Kim, Y. Mo and G. Ceder, *Nat. Mater.*, 2015, **14**, 1026.
57 S. P. Culver, R. Koerver, T. Krauskopf and W. G. Zeier, *Chem. Mater.*, 2018, **30**, 4179–4192.
58 C. Dietrich, M. Sadowski, S. Sicolo, D. A. Weber, S. J. Sedlmaier, K. S. Weldert, S. Indris, K. Albe, J. Janek and W. G. Zeier, *Chem. Mater.*, 2016, **28**, 8764–8773.
59 F. Ning, B. Xu, J. Shi, H. Su, M. Wu, G. Liu and C. Ouyang, *J. Mater. Chem. A*, 2017, **5**, 9618–9626.
60 M. Leslie and N. J. Gillan, *J. Phys. C: Solid State Phys.*, 1985, **18**, 973.
61 C. Freysoldt, J. Neugebauer and C. G. Van de Walle, *Phys. Rev. Lett.*, 2009, **102**, 016402.